small
NANO MICRO

MnO2 Nanosheets

Birnessite-Type MnO_2 Nanosheets with Layered Structures Under High Pressure: Elimination of Crystalline Stacking Faults and Oriented Laminar Assembly

Yugang Sun, Lin Wang, Yuzi Liu, and Yang Ren*

Ultrathin 2D nanosheets made of materials with layered crystalline structures (e.g., graphene,[1–11] silicane,[12–14] germanane,[15–19] transition metal dichalcogenides,[20–24] boron nitride,[25–27] etc.) have been extensively studied in the past several years due to their intriguing properties in both fundamental research and technological development. The wide exploration of various 2D materials benefits from the rapid pace of progress in graphene and the methodology developed in preparing ultrathin layers.[28,29] Similar to the mass-productive graphene from graphite, one of the most effective method is exfoliation of the 2D materials in liquid solutions by intercalating small ions (e.g., K^+, Na^+, Li^+, H^+) with the assistance of ultrasonication.[30–33] On the other hand, ultrathin 2D nanosheets of some materials (e.g., metal sulphides)[34] can be also synthesized via the bottom-up wet chemical strategy, in which small ions released from the reaction precursors are also possibly intercalated into the layered structures. The intercalation of small ions in the 2D materials can alternate their layered crystalline structures, leading to the generation of stacking faults that are indicated by the asymmetry of X-ray diffraction (XRD) peaks.[35–37] The stacking faults influence the long-range correlations across the crystalline layers in 2D crystallites, leading to a detrimental impact in their transportation properties (e.g., thermal conductivity, electronic conductivity, etc.) along the through-layer direction.[38–40] For example, stacking faults in a few-layer graphene electronically decouple individual layers from one another, and consequentially each graphene layer in the few-layer graphene displays a monolayer-like electronic structure.[39]

Among these 2D materials, nanosheets of birnessite-type manganese dioxide (MnO_2) have been widely studied because MnO_2 and derivatives represent a class of benchmark electrode materials for electrochemical energy storage devices including supercapacitors, lithium-ion batteries, and lithium-air batteries.[41–44] In general, many nanostructured allotropes of MnO_2 exist due to a large variety of possible crystallographic structures (e.g., α, β, δ, γ, and λ forms) and morphologies (e.g., plates, urchin-like architectures, flowers, cubes, wires, rods, belts, hollow spheres, etc.).[45,46] Therefore, synthesis of ultrathin MnO_2 nanosheets with a single high-purity crystallographic phase is challenging due to their high sensitivity towards reaction conditions. Herein we report the synthesis of birnessite-type MnO_2 nanosheets through a hydrothermal reduction of acidic $KMnO_4$ in an aqueous solution with the assistance of microwave heating. The as-synthesized MnO_2 nanosheets exhibit a layered crystalline structure (i.e., δ-phase) with a significant amount of lattice stacking faults. Surprisingly the lattice stacking faults can be completely removed by mechanically compressing the MnO_2 nanosheets. The compression does not change the overall crystallinity of the nanosheets although phase transition of MnO_2 nanostructures can easily occur at elevated temperatures due to the large numbers of MnO_2 allotropes.

Different MnO_2 nanostructures can be synthesized through the reduction of an aqueous $KMnO_4$ solution under carefully controlled reaction conditions. For example, mixing $KMnO_4$ with an aqueous solution of HCl followed by increasing the solution temperature favors the redox reaction:

$$2KMnO_4(aq) + 8HCl(aq) \rightarrow 2MnO_2(s) + 3Cl_2(g) + 2KCl(aq) + 4H_2O. \quad (1)$$

Apparently the reaction results in the formation of solid MnO_2 particles that are dispersed in the reaction solution

Dr. Y. Sun, Dr. Y. Liu
Center for Nanoscale Materials
Argonne National Laboratory
9700, South Cass Avenue, Argonne,
Illinois 60439, USA
E-mail: ygsun@anl.gov
Dr. L. Wang
HPSync, Geophysical Laboratory
Carnegie Institute of Washington
Argonne, Illinois 60439, USA
Dr. L. Wang
State Key Laboratory of Superhard Materials
Jilin University
Changchun 130012, China
Dr. L. Wang
Center for High Pressure Science and Technology Advanced Research
1690 Cailun Rd, Pudong District, Shanghai 201203, China
Dr. Y. Ren
X-Ray Science Division
Advanced Photon Source
Argonne National Laboratory
9700 South Cass Avenue, Argonne, Illinois 60439, USA

DOI: 10.1002/smll.201400892

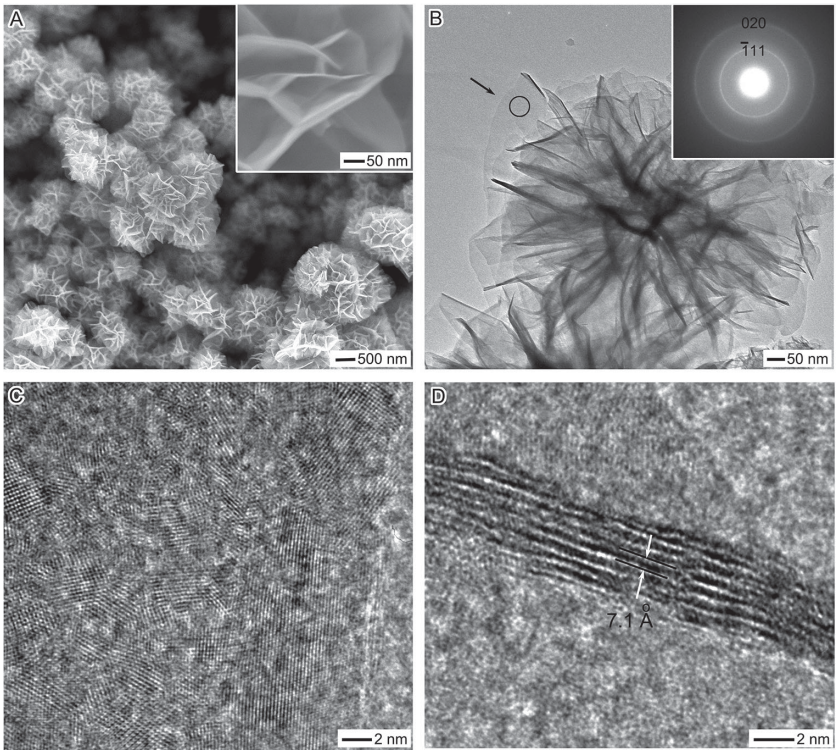

Figure 1. Characterization of the as-synthesized birnessite-type δ-phase MnO_2 microflowers containing interconnected ultrathin nanosheets. (A) SEM image of randomly assembled microflowers. The inset highlights the thin thicknesses of the MnO_2 nanosheets. (B) TEM image of an individual microflower. Electron diffraction pattern (inset, B) and (C) HRTEM image of a small portion of a nanosheet highlighted in the circle in (B). (D) HRTEM image of the edge of an individual nanosheet taken by aligning the electron beam parallel to the basal surfaces of the nanosheet. The arrows highlight the interplanar spacing in the δ-phase MnO_2 lattice.

and Cl_2 gas that is released from the solution. In the synthesis of birnessite-type MnO_2 nanosheets, an aqueous solution containing both $KMnO_4$ (0.055 M) and HCl (0.2 M) is heated up to 150 °C in a sealed reactor with a CEM microwave synthesizer. The heating ramp is set to take ~1 min to reach 150 °C at which the reaction lasts 5 min. The reaction leads to the formation of a black dispersion due to the formation of MnO_2 particles. Scanning electron microscopy (SEM) images of the black powders show that they are microspheres with a "desert rose"-like morphology and each microsphere is made of interconnected ultrathin nanosheets (**Figure 1**A). The formation of interesting morphology might be ascribed to the quick nucleation that tends to generate polycrystalline nuclei including multiple domains with different crystalline orientations. Since the MnO_2 crystallites formed from this reaction have an anisotropic crystalline structure (discussed in the following content), continuous growth of the polycrystalline nuclei will form interconnected MnO_2 nanosheets orientated in many different directions, i.e., "desert-rose" like microsphere. Similar morphologies have also been observed in the synthesis of urchinlike pyrolusite, γ-MnO_2, and Na-OMS-2 (OMS: octahedral molecular sieve) nanostructures.[47] The sizes of the microspheres are in the range of 1–2 μm. High-magnification SEM images of the nanosheets show that the individual nanosheets in the microspheres exhibit thicknesses ranging from 2 to 10 nm (inset, Figure 1A). The low imaging contrast of the nanosheets in the transmission electron microscopy (TEM) images also confirms the thin thickness of the nanosheets (Figure 1B). In addition, the single nanosheet (as highlighted by the arrow) lying on the TEM grid show a highly uniform imaging contrast across the sheet, indicating its uniform thickness. The high-resolution TEM (HRTEM) image obtained by aligning the electron beam perpendicular to the basal surfaces of a single nanosheet reveals that each nanosheet is an assembly of many crystalline domains with sizes less than 5 nm (Figure 1C). The HRTEM image recorded by aligning the electron beam parallel to the basal surfaces of a nanosheet at its edge clearly shows the parallel lattice fringes without interconnections (Figure 1D), indicating that the polycrystalline nanosheets have a layered crystalline structure with a interlayer spacing of ~7.1 Å. X-ray diffraction (XRD) pattern of the microspheres shown in Figure 1 exhibits reflection peaks that are consistent with the δ-phase of birnessite-type MnO_2 (**Figure 2**). The (001) and (002) peaks are intense and symmetric and they are reflections of the same lattice orientation at different diffraction orders. Comparison with the standard XRD pattern of the δ-phase MnO_2 reveals that these two peaks correspond to the layered structure of the δ-MnO_2. The lattice spacing along (001) direction is calculated to be 7.2 Å that is consistent

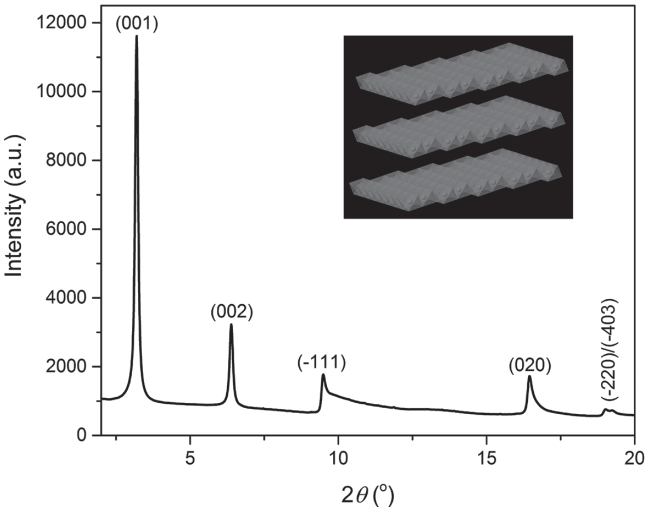

Figure 2. XRD pattern of the as-synthesized MnO_2 nanosheets recorded at a synchrotron X-ray beam line with an x-ray beam wavelength of 0.4066 Å. The peaks were assigned to the standard diffraction pattern of the layered δ-phase MnO_2 as shown in the inset. Due to the relatively large spacing and weak interactions between the crystalline layers, small cations (e.g., H^+, K^+) and molecules (e.g., H_2O) can be intercalated into the interlayered gaps, leading to the generation of stacking faults.

small 2014,
DOI: 10.1002/smll.201400892

small NANO MICRO

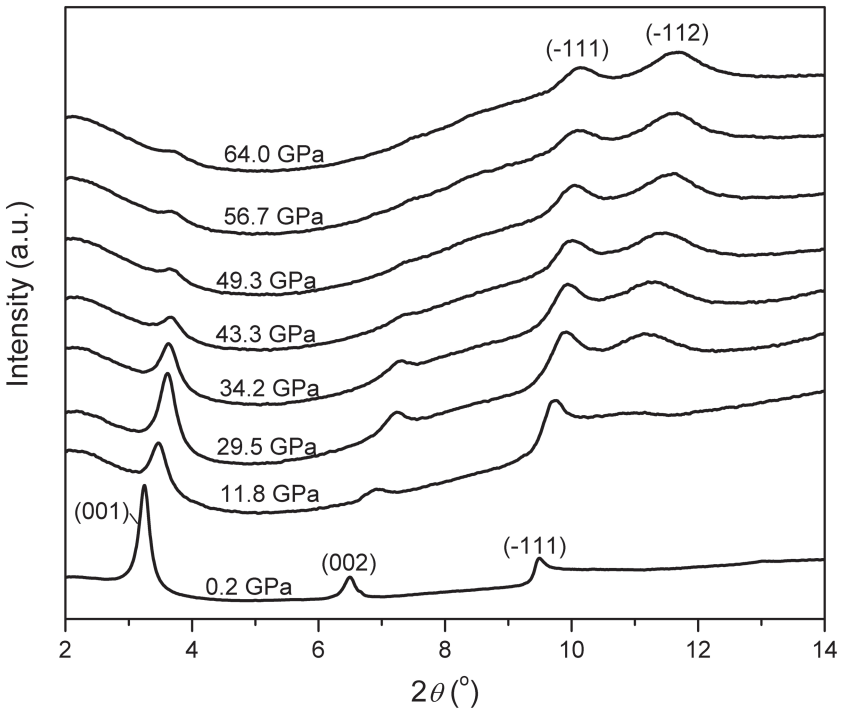

Figure 3. XRD patterns of the MnO_2 microflowers shown in Figure 1 measured during nonhydrostatic compression in a DAC under different pressures (i.e., the numbers associated with each pattern). The wavelength of the X-ray beam was 0.4066 Å. The patterns were offset for visional clarity.

with the interlayer spacing (i.e., ~7.1 Å) measured from the side-view of a MnO_2 nanosheet shown in Figure 1D. This consistency confirms that the imaged region of Figure 1D is the right sample. The high intensity and peak symmetry indicates that the in-plane lattices in each crystalline layers (i.e., the *a*-*b* planes) are well defined. In contrast, other diffraction peaks at high angles, e.g., those indexed with non-zero *h* and *k* Miller indices (for example, (-111) and (020) reflections), are asymmetric with apparent diffusive tails. The peak tailing of the (-111) and (020) peaks is ascribed to the significant stacking faults originated from lattice misalignment between different crystalline layers in the MnO_2 nanocrystals. In the synthesis solution there are high concentration of K^+ and H^+ cations, which can be trapped in the large interlayer gaps (>5 Å) in the δ-phase MnO_2 nanocrystals (insert, Figure 2).[48–50] Energy-dispersive X-ray spectroscopy (EDX) analysis of the MnO_2 nanosheets clearly shows the presence of K (Supplementary Information, Figure S1). In some cases intercalation of H_2O molecules between the crystalline MnO_2 layers is also possible.[48] Existence of the extra K^+, H^+ and H_2O molecules can easily disturb the weak bonding energy between the crystalline layers, leading to the observation of stacking faults caused by sliding of crystalline layers parallel to the basal surfaces along both *a* and *b* directions and possible expansion along *c* direction.

Dry powders of the synthesized δ-phase MnO_2 microspheres have been compressed in a diamond anvil cell (DAC) and the corresponding XRD patterns at different pressures are shown in **Figure 3**. The diffraction peaks become broader with the increase of compressive pressure due to the increased lattice strain in the MnO_2 nanocrystals and the possible fragmentation of the crystalline domains. Meanwhile all the peaks shift to the higher angles because of the reduced *d* spacing at high pressures. The *d* values along different crystallographic directions decrease with increase of external pressure by following non-linear functions (Supplementary Information, Figure S2). The *d* value along (001) directions decreases faster than that along (-111) and (-112) directions. The intensities of (001) and (002) peaks monotonically decrease and these two peaks are barely observed at very high pressures (e.g., 64.0 GPa). In contrast, the intensity of (-111) peak does not show significant variations as the compressive pressure increases. It is worthy of note that the (-111) peak becomes more symmetric with increase of pressure. A new peak that is assigned to (-112) reflections starts to emerge at pressures higher than ~10 GPa and becomes stronger with the continuous increase of the external pressure. The newly developed (-112) peak also shows high symmetry. However, The (-112) reflections are very weak for the as-synthesized δ-phase MnO_2 microspheres (Figure 1) and are overlapped with the strong tail of the major (-111) peak, leading to a difficulty to identify this peak in the XRD pattern (Figure 2 and the bottom curve in Figure 3). The improved symmetry of the (-111) peak and the appearance of the symmetric (-112) peak at high pressures can be attributed

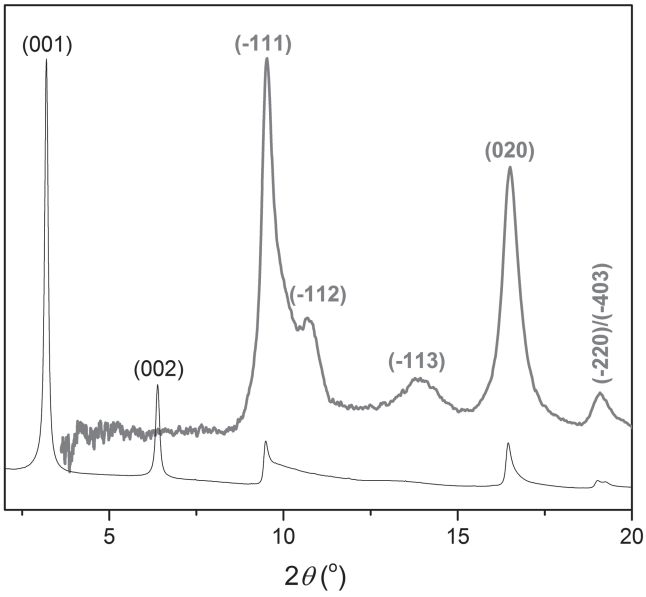

Figure 4. XRD pattern (upper thick curve) of the compressed MnO_2 microflowers after the pressure was released. The peaks are consistent with the standard diffraction pattern of δ-phase MnO_2. The XRD pattern (bottom thin curve) of the as-synthesized sample shown in Figure 1 was also plotted in the same figure for easy comparison.

DOI: 10.1002/smll.201400892

to the significant reduction of stacking faults between the crystalline layers in the δ-phase MnO_2 nanosheets. After the external pressure is slowly removed, the compressed MnO_2 microspheres is exposed to the ambient pressure and the corresponding XRD pattern is shown in **Figure 4** (thick curve). Taking the metal gasket (including the compressed MnO_2 sample) out of the DAC allows us to collect XRD signals in a wider range of diffraction angles. In the range of $2\theta >$ 7.5°, more diffraction peaks with significantly improved symmetry are observed in comparison with the XRD pattern of the as-synthesized MnO_2 nanosheets. In particular, the long tail of the (-111) peak of the original sample essentially disappears after high-pressure compression. Instead, the (-112) and (-113) reflections buried in the tail are developed into well-defined symmetric peaks. The asymmetric (020) peak of the original sample also becomes highly symmetric after high-pressure compression. The increased peak symmetry and observation of the new peaks are consistent with the XRD patterns recorded at high pressures, at which the lattice stacking faults between the crystalline layers in the δ-phase MnO_2 nanosheets are significantly eliminated. The consistence of the XRD patterns indicates that the crystalline structures with less stacking faults formed at high pressures can be maintained even after the compressive forces are removed. Careful comparison reveals that the peak widths of the (-111) and (020) peaks become broader after high-pressure compression, indicating that the MnO_2 crystalline domains might be fragmented into smaller grains. As a result, the originally overlapped (-220) and (-403) peaks appears as one very broad peak in the compressed sample.

The completely disappeared (002) peak at very high pressures cannot be recovered at all even after the pressure is released. The diffraction signals at the position of the (001) peak cannot be collected due to the limitation of experiment setup. It is believed that the compressed sample is not able to diffract X-ray by the (001) lattices because of the direct correlation of (001) and (002) reflections. The absence of the (001) and (002) diffraction peaks in the XRD pattern is similar to the electron diffraction patterns (inset, Figure 1B) obtained by aligning the electron beam perpendicular to the basal surfaces of individual nanosheets. Therefore, the disappearance of (001) and (002) peaks in the compressed sample might be caused by re-orientating the MnO_2 nanosheets to align their basal surfaces perpendicular to the X-ray beam. The compressed sample has been studied with TEM. **Figure 5**A shows a typical TEM image with a dimension comparable to the size of an individual MnO_2 microsphere shown in Figure 1B. The morphology of the materials and the distribution of

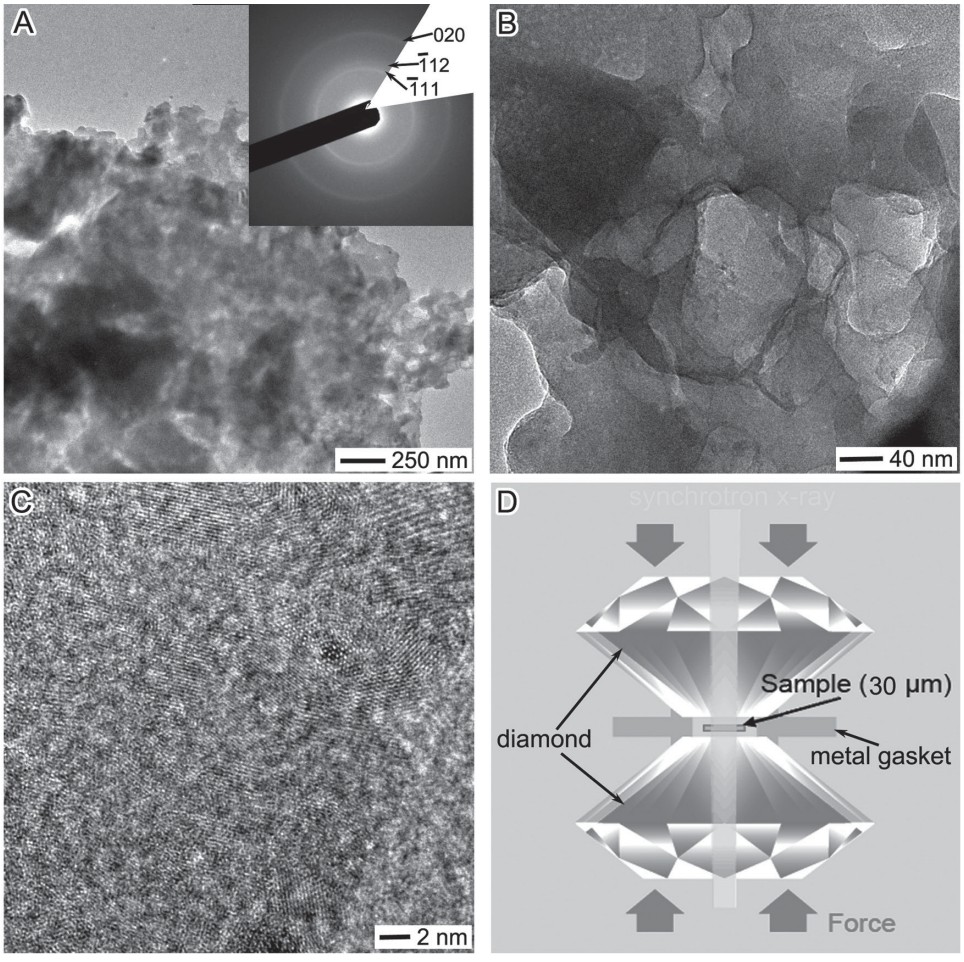

Figure 5. TEM micrographs (A-C) and the corresponding selected area electron diffraction pattern (inset, A) of the compressed MnO_2 nanosheets after they relaxed to the ambient pressure (i.e., 1 bar). (D) Schematic illustration of the experiment setup, highlighting the orientation of the compressive force and the X-ray beam.

small 2014,
DOI: 10.1002/smll.201400892

NANO MICRO small

imaging contrast shown in Figure 5A are significantly different from the original flower-like MnO_2 microspheres, indicating that the random orientations of the interconnected MnO_2 nanosheets in the microspheres no longer exist after high-pressure compression. TEM images with high magnifications of the compressed sample reveal that the nanosheets are packed in a layer-by-layer fashion (Figure 5B). This layer-by-layer assembly forces all of the nanosheets to orientate their basal surfaces perpendicular to the direction of the external compressive force. HRTEM images (Figure 5C) of the compressed sample exhibit a polycrystalline feature similar to the as-synthesized MnO_2 nanosheets shown in Figure 1C. The similarity indicates that high-pressure compression does not significantly influence the in-plane lattice crystallinity in the MnO_2 nanosheets despite of removal of the through-plane stacking faults. As shown in Figure 5D, the X-ray beam is parallel to the force direction and thus perpendicular to the basal surfaces of all packed nanosheets. Similar to the electron diffraction pattern shown in Figure 1B, the alignment of all the nanosheets in the DAC disables the (001) and (002) lattices of the δ-MnO_2 nanocrystals to diffract the X-ray. The corresponding electron diffraction pattern obtained from the compressed sample does not show the (001) and (002) reflections. Similar to the electron diffraction pattern of a single nanosheet, strong diffraction rings of the (-111) and (020) reflections are also observed from the compressed sample (inset, Figure 5A). In addition, the (-112) reflections are significantly enhanced to display as a well-identified ring due to the elimination of crystalline stacking faults in the δ-MnO_2 nanocrystals.

In summary, birnessite-type MnO_2 microspheres composed of interconnected δ-phase polycrystalline nanosheets has been synthesized via a microwave-assistant hydrothermal process and their behaviors under high pressures have been studied in an in-situ DAC with synchrotron X-ray diffraction. Because of the anisotropic two-dimension platelet morphology of the MnO_2 nanosheets, the randomly oriented nanosheets become ordered assembly with a layer-by-layer fashion upon exposure to very high compressive pressures. The crystalline stacking faults in the δ-phase MnO_2 nanocrystals are significantly eliminated when the pressure reaches a critical value. Nanocrystals with crystalline stacking faults usually represent a metastable structure compared to nanocrystals with perfect lattices. As a result, applying external stimuli to the nanocrystals with stacking faults can overcome an energy barrier to transform the defective nanocrystals to perfect ones. The results presented in Figure 3 clearly show that high compressive forces can overcome the energy barrier to eliminate crystalline stacking faults from the colloidal δ-phase MnO_2 nanosheets to increase their crystalline perfection. It is important to point out that the external compressive forces only perfect the crystalline lattices without changing the basic layered crystalline structures and morphology of the δ-phase MnO_2 nanosheets. In contrast, other stimuli such as high-temperature annealing usually transform the δ-phase MnO_2 nanosheets to products with different crystalline structures (e.g., α-phase MnO_2 with tunnel lattices) and morphologies (e.g., nanowires, nanotubes, etc.).[46,51] This high-pressure strategy might be extended to reduce stacking faults of other colloidal nanomaterials with layered crystalline structures.

Experimental Section

Synthesis of δ-Phase MnO_2 Microspheres: The spherical microflowers made of δ-phase MnO_2 nanosheets were synthesized through a microwave-assistant hydrothermal process in which an aqueous solution containing both potassium permanganate ($KMnO_4$) and hydrochloric acid (HCl) in a sealed reactor was heated with controlled microwave radiation in a commercial CEM Discover system. In a typical synthesis, $KMnO_4$ powders (52.6 mg, Sigma-Aldrich) and a HCl aqueous solution (1 mL, 1.2 M, Sigma-Aldrich) were added to deionized water (5 mL). The mixture was then sealed in a 10-mL glass-tube reaction vessel with a silicone septum. Placing the reaction vessel in the microwave cavity enabled heating the solution to 150 °C within ~1 min. Continuously heating the solution for an additional 5 min at 150 °C led to a completion of the redox reaction between $KMnO_4$ and HCl, resulting in the formation of microflowers made of δ-phase MnO_2 nanosheets. The reaction solution was then quickly cooled down to room temperature with a nitrogen blow. The resulting black dispersion was centrifuged, washed with deionized water, and the collected black powders were dried in an oven set at 60 °C in air.

High-Pressure Measurement of the MnO_2 Microspheres: A Mao-Bell-type DAC was used to generate high pressure in the sample.[52] In a typical measurement, the sample chamber was created by drilling a hole (~100 μm in diameter) in a pre-indented stainless steel gasket (~30 μm in thickness). No pressure medium was used in the high-pressure measurements. Pressures were determined from the fluorescent spectra of the ruby chips loaded into the sample chamber.[53] The in-situ high-pressure XRD experiments were carried out at 16ID-B station and the ex-situ XRD experiments were carried out at 16BM-D station of the High Pressure Collaborative Access Team (HPCAT), Advanced Photon Source, Argonne National Laboratory. The energy of X-ray for the measurements was 30.491 keV. The diffraction patterns were collected with 2D imaging plates. FIT2D was used to process the diffraction data.

Characterization of the Synthesized and Compressed MnO_2 Nanoplates: SEM images were recorded on a JEOL JSM-7500F field emission scanning electron microscope. TEM images and electron diffraction patterns were taken on a JEOL-JEM-2100F microscope operating at a voltage of 200 kV.

Supporting Information

Supporting Information is available from the Wiley Online Library or from the author.

Acknowledgements

This work was performed at the Center for Nanoscale Materials, a U.S. Department of Energy, Office of Science, Office of Basic Energy Sciences User Facility under contract No. DE-AC02–06CH11357.

Use of Advanced Photon Source (beamline 11ID-C, 16ID-B, 16BM-D) was supported by the U.S. Department of Energy, Office of Science, Office of Basic Energy Sciences, under contract No. DE-AC02–06CH11357. HPCAT is supported by CIW, CDAC, UNLV and LLNL through funding from DOE-NNSA, DOE-BES, and NSF. Lin Wang is supported by EFree, an Energy Frontier Research Center funded by the U.S. Department of Energy (DOE), Office of Science under DE-SC0001057, the National Natural Science Foundation of China (NSFC, 11004072) and Program for New Century Excellent Talents in University (NCET-10–0444).

[1] K. S. Novoselov, A. K. Geim, S. V. Morozov, D. Jiang, Y. Zhang, S. V. Dubonos, I. V. Grigorieva, A. A. Firsov, *Science* **2004**, *306*, 666–669.
[2] K. S. Novoselov, A. K. Geim, S. V. Morozov, D. Jiang, M. I. Katsnelson, I. V. Grigorieva, S. V. Dubonos, A. A. Firsov, *Nature* **2005**, *438*, 197–200.
[3] S. X. Wu, Q. Y. He, C. L. Tan, Y. D. Wang, H. Zhang, *Small* **2013**, *9*, 1160–1172.
[4] X. Huang, Z. Y. Zeng, Z. X. Fan, J. Q. Liu, H. Zhang, *Adv. Mater.* **2012**, *24*, 5979–6004.
[5] S. Han, D. Q. Wu, S. Li, F. Zhang, X. L. Feng, *Small* **2013**, *9*, 1173–1187.
[6] D. M. Sun, C. Liu, W. C. Ren, H. M. Cheng, *Small* **2013**, *9*, 1188–1205.
[7] H. X. Wang, Q. Wang, K. G. Zhou, H. L. Zhang, *Small* **2013**, *9*, 1266–1283.
[8] G. C. Xie, K. Zhang, B. D. Guo, Q. Liu, L. Fang, J. R. Gong, *Adv. Mater.* **2013**, *25*, 3820–3839.
[9] W. G. Xu, N. N. Mao, J. Zhang, *Small* **2013**, *9*, 1206–1224.
[10] D. Zhan, J. X. Yan, L. F. Lai, Z. H. Ni, L. Liu, Z. X. Shen, *Adv. Mater.* **2012**, *24*, 4055–4069.
[11] Y. Zhu, D. K. James, J. M. Tour, *Adv. Mater.* **2012**, *24*, 4924–4955.
[12] O. D. Restrepo, R. Mishra, J. E. Goldberger, W. Windl, *J. Appl. Phys.* **2014**, *115*, 033711 .
[13] J. Wang, J. B. Li, S. S. Li, Y. Liu, *J. Appl. Phys.* **2013**, *114*, 124309.
[14] L. C. L. Y. Voon, E. Sandberg, R. S. Aga, A. A. Farajian, *Appl. Phys. Lett.* **2010**, *97*, 163114.
[15] E. Bianco, S. Butler, S. S. Jiang, O. D. Restrepo, W. Windl, J. E. Goldberger, *ACS Nano* **2013**, *7*, 4414–4421.
[16] K. J. Koski, Y. Cui, *ACS Nano* **2013**, *7*, 3739–3743.
[17] M. Houssa, E. Scalise, K. Sankaran, G. Pourtois, V. V. Afanas'ev, A. Stesmans, *Appl. Phys. Lett.* **2011**, *98*, 223107.
[18] O. Pulci, P. Gori, M. Marsili, V. Garbuio, R. Del Sole, F. Bechstedt, *EPL* **2012**, *98*, 37004.
[19] Y. D. Ma, Y. Dai, Y. B. Lu, B. B. Huang, *J. Mater. Chem. C* **2014**, *2*, 1125–1130.
[20] M. Chhowalla, H. S. Shin, G. Eda, L. J. Li, K. P. Loh, H. Zhang, *Nat. Chem.* **2013**, *5*, 263–275.
[21] Q. H. Wang, K. Kalantar-Zadeh, A. Kis, J. N. Coleman, M. S. Strano, *Nat. Nanotechnol.* **2012**, *7*, 699–712.
[22] H. Li, G. Lu, Z. Y. Yin, Q. Y. He, H. Li, Q. Zhang, H. Zhang, *Small* **2012**, *8*, 682–686.
[23] H. Matte, A. Gomathi, A. K. Manna, D. J. Late, R. Datta, S. K. Pati, C. N. R. Rao, *Angew. Chem.-Int. Edit.* **2010**, *49*, 4059–4062.
[24] W. J. Yu, Y. Liu, H. L. Zhou, A. X. Yin, Z. Li, Y. Huang, X. F. Duan, *Nat. Nanotechnol.* **2013**, *8*, 952–958.
[25] M. P. Levendorf, C. J. Kim, L. Brown, P. Y. Huang, R. W. Havener, D. A. Muller, J. Park, *Nature* **2012**, *488*, 627–632.
[26] Y. Kobayashi, K. Kumakura, T. Akasaka, T. Makimoto, *Nature* **2012**, *484*, 223–227.
[27] R. V. Gorbachev, I. Riaz, R. R. Nair, R. Jalil, L. Britnell, B. D. Belle, E. W. Hill, K. S. Novoselov, K. Watanabe, T. Taniguchi, A. K. Geim, P. Blake, *Small* **2011**, *7*, 465–468.
[28] J. Y. Luo, J. Kim, J. X. Huang, *Accounts Chem. Res.* **2013**, *46*, 2225–2234.
[29] D. Li, R. B. Kaner, *Science* **2008**, *320*, 1170–1171.
[30] Z. Y. Zeng, T. Sun, J. X. Zhu, X. Huang, Z. Y. Yin, G. Lu, Z. X. Fan, Q. Y. Yan, H. H. Hng, H. Zhang, *Angew. Chem.-Int. Edit.* **2012**, *51*, 9052–9056.
[31] J. Heising, M. G. Kanatzidis, *J. Am. Chem. Soc.* **1999**, *121*, 11720–11732.
[32] V. Nicolosi, M. Chhowalla, M. G. Kanatzidis, M. S. Strano, J. N. Coleman, *Science* **2013**, *340*, 1420.
[33] K. Lee, H. Y. Kim, M. Lotya, J. N. Coleman, G. T. Kim, G. S. Duesberg, *Adv. Mater.* **2011**, *23*, 4178.
[34] Y. Du, Z. Yin, J. Zhu, X. Huang, X.-J. Wu, Z. Zeng, Q. Yan, H. Zhang, *Nat. Commun.* **2012**, *3*, 1177.
[35] C. Altavilla, M. Sarno, P. Ciambelli, A. Senatore, V. Petrone, *Nanotechnology* **2013**, *24*, 125601.
[36] K. H. Hu, X. G. Hu, J. D. Sun, *J. Mater. Sci.* **2010**, *45*, 2640–2648.
[37] C. S. Rout, P. D. Joshi, R. V. Kashid, D. S. Joag, M. A. More, A. J. Simbeck, M. Washington, S. K. Nayak, D. J. Late, *Sci. Rep.* **2013**, *3*, 3282.
[38] J. N. Shapiro, A. Lin, C. Ratsch, D. L. Huffaker, *Nanotechnology* **2013**, *24*, 475601.
[39] B. J. Schultz, R. V. Dennis, V. Lee, S. Banerjee, *Nanoscale* **2014**, *6*, 3444.
[40] X. Tian, M. E. Itkis, E. B. Bekyarova, R. C. Haddon, *Sci. Rep.* **2013**, *3*, 1710.
[41] W. Wei, X. Cui, W. Chen, D. G. Ivey, *Chem. Soc. Rev.* **2011**, *40*, 1697–1721.
[42] X. Lang, A. Hirata, T. Fujita, M. Chen, *Nat. Nanotechnol.* **2011**, *6*, 232–236.
[43] A. Débart, A. J. Paterson, J. Bao, P. G. Bruce, *Angew. Chem. Int. Ed.* **2008**, *47*, 4521–4524.
[44] P. G. Bruce, S. A. Freunberger, L. J. Hardwick, J.-M. Tarascon, *Nat. Mater.* **2012**, *11*, 19–29.
[45] P. Ragupathy, D. H. Park, G. Campet, H. N. Vasan, S.-J. Hwang, J.-H. Choy, N. Munichandraiah, *J. Phys. Chem. C* **2009**, *113*, 6303–6309.
[46] T. T. Truong, Y. Liu, Y. Ren, L. Trahey, Y. Sun, *ACS Nano* **2012**, *6*, 8067–8077.
[47] W.-N. Li, J. Yuan, X.-F. Shen, S. Gomez-Mower, L.-P. Xu, S. Sithambaram, M. Aindow, S. L. Suib, *Adv. Funct. Mater.* **2006**, *16*, 1247.
[48] X. Yang, Y. Makita, Z.-h. Liu, K. Sakane, K. Ooi, *Chem. Materi.* **2004**, *16*, 5581–5588.
[49] P. K. Nayak, T. R. Penki, N. Munichandraiah, *J. Electroanal. Chem.* **2013**, *703*, 126–134.
[50] A. Ogata, S. Komaba, R. Baddour-Hadjean, J. P. Pereira-Ramos, N. Kumagai, *Electrochim. Acta* **2008**, *53*, 3084–3093.
[51] Y. G. Sun, Y. Z. Liu, T. T. Truong, Y. Ren, *Sci. China Chem.* **2012**, *55*, 2346–2352.
[52] H. K. Mao, P. M. Bell, *Carnegie Inst. Washington Yearb.* **1975**, *74*, 402–405.
[53] H. K. Mao, J. Xu, P. M. Bell, *J. Geophys. Res.-Solid Earth and Planets* **1986**, *91*, 4673–4676.

Received: April 1, 2014
Revised: July 8, 2014
Published online:

DOI: 10.1002/smll.201400892